


Article

Modeling Atom Interferometry Experiments with Bose–Einstein Condensates in Power-Law Potentials

Stephen Thomas ¹, Colson Sapp ¹, Charles Henry ¹, Andrew Smith ¹, Charles A. Sackett ² , Charles W. Clark ^{3,4}  and Mark Edwards ^{1,*} 

¹ Department of Physics and Astronomy, Georgia Southern University, Statesboro, GA 30458, USA; st04260@georgiasouthern.edu (S.T.); rs06305@georgiasouthern.edu (C.S.); ch12779@georgiasouthern.edu (C.H.); as06061@georgiasouthern.edu (A.S.)

² Department of Physics, University of Virginia, Charlottesville, VA 22904, USA; sackett@virginia.edu

³ Joint Quantum Institute, University of Maryland, College Park, MD 20742, USA; charles.winthrop.clark@gmail.com

⁴ National Institute of Standards and Technology, University of Maryland, College Park, MD 20742, USA

* Correspondence: edwards@georgiasouthern.edu

Abstract: Recent atom interferometry (AI) experiments involving Bose–Einstein condensates (BECs) have been conducted under extreme conditions of volume and interrogation time. Numerical solution of the rotating-frame Gross–Pitaevskii equation (RFGPE), which is the standard mean-field theory applied to these experiments, is impractical due to the excessive computation time and memory required. We present a variational model that provides approximate solutions of the RFGPE for a power-law potential on a practical time scale. This model is well-suited to the design and analysis of AI experiments involving BECs that are split and later recombined to form an interference pattern. We derive the equations of motion of the variational parameters for this model and illustrate how the model can be applied to the sequence of steps in a recent AI experiment where BECs were used to implement a dual-Sagnac atom interferometer rotation sensor. We use this model to investigate the impact of finite-size and interaction effects on the single-Sagnac-interferometer phase shift.

Keywords: atom interferometer; Bose–Einstein condensate; Gross–Pitaevskii equation



Citation: Thomas, S.; Sapp, C.; Henry, C.; Smith, A.; Sackett, C.A.; Clark, C.W.; Edwards, M. Modeling Atom Interferometry Experiments with Bose–Einstein Condensates in Power-Law Potentials. *Atoms* **2022**, *10*, 34. <https://doi.org/10.3390/atoms10010034>

Academic Editor: Andrea Bertoldi

Received: 8 December 2021

Accepted: 28 February 2022

Published: 21 March 2022

Publisher’s Note: MDPI stays neutral with regard to jurisdictional claims in published maps and institutional affiliations.



Copyright: © 2022 by the authors. Licensee MDPI, Basel, Switzerland. This article is an open access article distributed under the terms and conditions of the Creative Commons Attribution (CC BY) license (<https://creativecommons.org/licenses/by/4.0/>).

1. Introduction

Ultracold atom interferometry (AI) has become a mature technology over the past 25 years [1]. Today, it has many applications, including precision metrology, quantum sensing, and tests of fundamental physics. Precision metrology applications include measurements of the fine-structure [2–5] and universal gravitation fundamental constants [6,7], geophysical measurements [8], and measuring the local acceleration of gravity as part of the new Kibble-balance kilogram standard [9,10]. AI quantum sensors measure rotation and acceleration for precision navigation [11–16] and serve as gravity gradiometers for geodesy and civil engineering [17]. Atom interferometers have also been proposed for gravity-wave detection [18–22]. Probes of fundamental physics include dark-matter and dark-energy searches [23–29] as well as tests of Einstein’s Equivalence Principle [30–36].

Many AI experiments involve splitting and recombining a Bose–Einstein condensate (BEC). Early measurements demonstrated that BECs were capable of interference [37–39]. More recently, BEC atom interferometers have been used for measuring the fine-structure constant [40] and as gravimeters [41]. Condensates have been used in interferometers on atom chips [42], have been confined in large ring potentials [43–46], and launched through waveguide painted-potentials [47]. Finally, extraterrestrial AI uses BEC as a source. In 2017, the MAIUS-1 sounding-rocket mission produced BEC and conducted AI experiments above the Kármán line, between 100 and 243 km above the Earth’s surface [48,49]. In 2020, a BEC of some 50,000 ⁸⁷Rb atoms was produced aboard the Earth-orbiting International Space Station [50]. There is an ongoing effort to implement BEC-enabled AI in that environment [51].

Using condensates in AI processes confers the advantages of narrow momentum distributions and better signals due to their higher density relative to above- T_c gases. Thus, using condensates in AIs hold high promise for accurate measurements [52]. High densities have the disadvantage that interactions can cause phase diffusion that tends to reduce the contrast of the interference pattern generated by overlapping BEC clouds [53]. Furthermore, mean-field repulsion of overlapping clouds can alter their relative velocity, which can change the frequency of the interference pattern [54]. Indeed, many BEC AI experiments use small condensates in order to minimize the effects of interactions. While there has been a good deal of theoretical work done on the effect of interactions in BEC AIs [52,55–57], few have used accurate solutions of the Gross–Pitaevskii equation (GPE) in their analysis.

The time-dependent Gross–Pitaevskii equation is the standard mean-field theory that governs the behavior of confined ultracold gases at near-zero temperatures [58]. There is every reason to think that it will apply to BEC AI systems even in the most extreme cases where the condensate is split into multiple high-momentum clouds, which are then allowed to separate to a distance that is orders of magnitude larger than the original condensate size and where the system evolution time is long. Precision solutions of the GPE should thus be able accurately to account for the effects of interactions. The reason that previous analyses of BEC AIs have not solved the GPE numerically is that the extreme conditions (large-momentum, large-volume, long interrogation times) of these AIs are beyond the current state of the art of known algorithms for solving the GPE on a practical timescale [59].

In this paper, we investigate the effects of atom–atom interactions and the presence of anharmonic potential terms on the operation of a dual-Sagnac atom interferometry rotation sensor. A version of this sensor was recently implemented in an experiment conducted at the University of Virginia. In this experiment a BEC, confined in a nominally harmonic potential, is split into two pairs of counter-orbiting condensates using laser light. Each pair constitutes a single Sagnac interferometer for sensing the frame rotation speed. The dual-Sagnac interferometer arrangement enables common-mode rejection of various noise sources while rotation affects the two interferometers oppositely. This experiment is described below and in more detail in Ref. [16]. Our goal in this work was to discover the physical mechanisms behind the effects of condensate size and anharmonic potentials on rotation sensor operation and to investigate how these effects depend on the interferometer area and frame rotation speed.

We assume that the behavior of the condensate in this experiment can be described by the rotating-frame Gross–Pitaevskii equation (RFGPE) [60]. Simulating this experiment by direct numerical solution of the RFGPE is impractical due to the large interferometer areas and long system evolution times involved. Future planned implementations of this rotation sensor design will need to increase these areas and times by 1–2 orders of magnitude to be competitive with the current state-of-the-art rotation sensors.

We have therefore obtained approximate solutions to the RFGPE using the Lagrangian Variational Method (LVM) [61,62]. The trial wave function that approximates the RFGPE solution is a sum of 3D Gaussian functions, one Gaussian for each separate cloud, having time-dependent widths and phases as variational parameters. Applying the LVM with this trial wave function to the experiment produces a system of coupled equations for these parameters. These equations can be used to model each step of the experimental sequence. The variational approximation enables us to simulate sensor operation even when the interferometer areas and condensate sizes are much larger than in the experiment.

The physical picture embodied in this approximation pictures the system as a set of Gaussian shaped condensate clouds. Each cloud moves along its own trajectory determined by the external potential and the repulsive interaction with other clouds when there is overlap. Furthermore, each cloud breathes in and out during its flight due to the interplay between the confining potential and the cloud’s internal repulsion. The model also accounts for minor width effects due to the interaction of different clouds when they overlap.

Condensate clouds pass through each other during the Virginia dual-Sagnac interferometer sequence. The effects of condensate collisions have been well-studied in previous

works [63–66]. These show that when BECs collide, vortex formation and dynamical instabilities can result. Here, however, the condensates are moving at a high relative velocity and are overlapped for only a short time. No vortex formation was observed in that experiment.

In the Virginia rotation sensor experiment [16], condensate atoms were confined in a TOP (time-averaged orbiting potential) trap potential. The TOP trap magnetic field is the superposition of a “gradient field” produced by two co-axial current-carrying coils in anti-Helmholtz configuration centered on the z axis plus a “bias field” that rotates rapidly in the xy plane. The bias field is produced by two pairs of co-axial coils with axes along x and y . This field rotates so rapidly that the potential (proportional to the time average of the magnitude of the total magnetic field) is nominally harmonic.

In their analysis of their original experiment [16] the experimentalists assumed that their TOP trap potential was purely harmonic. They later performed a more careful characterization of their potential and published the result in Ref. [67]. This characterization was based on a theoretical and experimental analysis of the magnetic fields produced by their TOP trap in their actual apparatus. The result was that, in addition to the harmonic terms assumed in analysis of their original experiment, there were anharmonic terms present in the potential. These anharmonic terms were found by performing a 3D Taylor expansion of the exact magnetic field produced by the TOP trap coils. The full potential therefore took the form of a power-law potential. We have used that potential in the work presented here.

In Section 2, we review the variational model and write down the equations of motion for the variational parameters. In Section 3, we present the AI sequence carried out in the dual-Sagnac rotation speed measurement. In Section 4, we write down the equations of motion for the variational parameters contained in trial wave condensate wave function. In Section 5, we derive exact expressions for the stopped-atom fraction in terms of the model variational parameters. This stopped-atom fraction is necessary for experimental extraction of the speed of the rotating frame from the data. In Section 6, we derive approximate formulas for this quantity for zero-rotation speed and for a harmonic potential when cloud–cloud interactions are neglected. In Section 7, we present the results of a set of simulations designed to study the effects of interactions and anharmonic terms in the potential. Finally, we summarize in Section 8.

2. Variational GPE Solver Model

We have developed and implemented [60] a variational model that provides rapid approximate solutions for the rotating-frame Gross–Pitaevskii equation (RFGPE) given by [58]

$$i\hbar \frac{\partial \Phi}{\partial t} = -\frac{\hbar^2}{2M} \nabla^2 \Phi + V_{\text{ext}}(\mathbf{r}, t) \Phi + g_{3D} N |\Phi|^2 \Phi + i\hbar \boldsymbol{\Omega} \cdot (\mathbf{r} \times \nabla) \Phi, \quad (1)$$

where $\Phi(\mathbf{r}, t)$ is the condensate wave function, M is the mass of a condensate atom, N is the number of atoms in the condensate, $g_{3D} = 4\pi\hbar^2 a_s / M$ measures the strength of the atom–atom scattering with a_s being the scattering length, $V_{\text{ext}}(\mathbf{r}, t)$ is the potential exerted on a condensate atom by external fields, and $\boldsymbol{\Omega}$ is the angular velocity of the rotating frame.

Our variational model is based on the Lagrangian Variational Method (LVM) [61,62], which provides equations of motion for time-dependent variational parameters appearing in a trial wave function. The equations of motion for these variational parameters are derived by integrating the Lagrangian density over all space yielding the ordinary Lagrangian and then using the standard Euler–Lagrange equations, to produce an equation of motion for each variational parameter.

In our model, the trial wave function represents each of the N_c wave packets as a 3D Gaussian. The mathematical form is the superposition:

$$\Psi(\mathbf{r}, t) = \frac{1}{\sqrt{N_c}} \sum_{j=1}^{N_c} A_j(t) e^{g_j(\mathbf{r}, t)} \quad (2)$$

where

$$g_j(\mathbf{r}, t) = \sum_{\eta=x,y,z} \left(-\frac{(\eta - \eta_j(t))^2}{2w_{j\eta}(t)^2} + i\epsilon_{j\eta}(t)\eta + i\beta_{j\eta}(t)\eta^2 \right). \quad (3)$$

The variational parameters are the center coordinates η_j , the widths $w_{j\eta}$, and linear $\epsilon_{j\eta}$ and quadratic $\beta_{j\eta}$ phase parameters for each cloud. These are indicated above as explicit functions of time.

Here, we make two assumptions about the physical system, which have material effects on the values of the variational parameters. These are as follows:

1. We assume that each of the N_c clouds are moving at sufficiently different velocities such that any integral of a quantity containing a factor like $\exp\{i(k_{j\eta} - k_{j'\eta})\eta\}$ where $j \neq j'$ can be neglected. If the clouds move with sufficiently different velocities, these factors will be rapidly oscillating and their integrals can be neglected.
2. The number of atoms in each cloud is fixed. Clouds do not lose or exchange atoms.

We can use these assumptions plus the normalization condition on the trial wave function to derive conditions that constrain the values of the A_j . Our assumption that the number of atoms in each cloud is fixed adds the further restriction that each cloud is individually normalized. The result is

$$|A_j(t)|^2 \pi^{3/2} w_{jx}(t) w_{jy}(t) w_{jz}(t) = 1, \quad j = 1, \dots, N_c. \quad (4)$$

The equations of motion are a pair of second-order ordinary differential equations for the cloud centers and widths as well as expressions for the $\beta_{j\eta}$ and the $\epsilon_{j\eta}$ in terms of the centers, widths and their first derivatives:

$$\ddot{x}_j = 2\Omega_z \dot{y}_j + \Omega_z^2 x_j - \frac{1}{M} \frac{\partial U^{(3D)}}{\partial x_j}, \quad (5a)$$

$$\ddot{y}_j = -2\Omega_z \dot{x}_j + \Omega_z^2 y_j - \frac{1}{M} \frac{\partial U^{(3D)}}{\partial y_j}, \quad (5b)$$

$$\ddot{z}_j = -\frac{1}{M} \frac{\partial U^{(3D)}}{\partial z_j}, \quad (5c)$$

$$\ddot{w}_{j\eta} = \frac{\hbar^2}{M^2} w_{j\eta}^{-3} - \frac{2}{M} \frac{\partial U^{(3D)}}{\partial w_{j\eta}}, \quad (5d)$$

$$\beta_{j\eta} = \frac{M}{2\hbar} \frac{\dot{w}_{j\eta}}{w_{j\eta}}, \quad (5e)$$

$$\epsilon_{jx} = \frac{M}{\hbar} (\dot{x}_j - \Omega_z y_j) - 2\beta_{jx} x_j, \quad (5f)$$

$$\epsilon_{jy} = \frac{M}{\hbar} (\dot{y}_j + \Omega_z x_j) - 2\beta_{jy} y_j, \quad (5g)$$

$$\epsilon_{jz} = \frac{M}{\hbar} \dot{z}_j - 2\beta_{jz} z_j, \quad (5h)$$

$$\eta = x, y, z \quad j = 1, \dots, N_c$$

The equations for the cloud centers and cloud widths (Equation (5a–d)) form a closed set that contain only the η_j , $\dot{\eta}_j$, $w_{j\eta}$, and $\dot{w}_{j\eta}$. Once these quantities are obtained, all of the other variational parameters can be calculated.

The factor $U^{(3D)}(\mathbf{x}, \mathbf{w})$ is the “variational potential”

$$U^{(3D)}(\mathbf{x}, \mathbf{w}) \equiv U_{\text{ext}}^{(3D)}(\mathbf{x}, \mathbf{w}) + U_{\text{int}}^{(3D)}(\mathbf{x}, \mathbf{w}). \quad (6)$$

The external and interaction variational potentials are the expectation values of the actual external potential and the condensate density over the trial wave function. The expression for $U_{\text{ext}}^{(3D)}(\mathbf{x}, \mathbf{w})$ is

$$U_{\text{ext}}^{(3D)}(\mathbf{x}, \mathbf{w}) \equiv N_c \int_{-\infty}^{\infty} dx \int_{-\infty}^{\infty} dy \int_{-\infty}^{\infty} dz \Psi^*(\mathbf{r}, t) V_{\text{ext}}(\mathbf{r}, t) \Psi(\mathbf{r}, t) \quad (7a)$$

$$= \sum_{j=1}^{N_c} \left(\frac{1}{\pi^{3/2} w_{jx} w_{jy} w_{jz}} \right) \int d^3r \exp \left\{ - \sum_{\eta=x,y,z} \frac{(\eta - \eta_j)^2}{w_{j\eta}^2} \right\} V_{\text{ext}}(\mathbf{r}, t). \quad (7b)$$

We note here that the variational potential definition given here is smaller than that defined in Ref. [60] by a factor of 2.

The equations of motion for the cloud centers and widths are valid for any external potential. This variational potential is only a function of the center and width parameters of all of the Gaussians. This model is capable of simulating extreme AI processes such as multiple high-momentum clouds, large volumes, and long interrogation times in a few minutes on a commodity desktop computer.

3. The Virginia Dual-Sagnac Atom-Interferometer Sequence

To illustrate how this variational model can be used to simulate an actual atom-interferometer sequence, we will apply it to a recent dual-Sagnac atom interferometer experiment conducted at the University of Virginia. The goal of this experiment was to implement a high-precision rotation sensor using a confined BEC [16].

The steps of this experiment are described in detail in Figure 1 are summarized here as follows. A BEC is formed in a nominally harmonic trap and is initially split by a pair of counter propagating laser pulses into two clouds along the $\pm y$ axis at velocities $\pm v_B \hat{\mathbf{y}}$ (First Split). The speed $v_B = 4\pi\hbar/(M\lambda_L)$ transfers the momentum of two laser photons to each condensate atom.

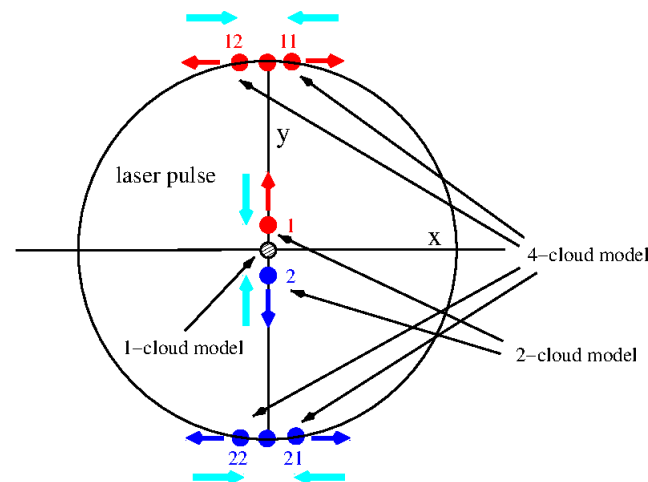


Figure 1. The Virginia dual Sagnac interferometer sequence as viewed from a non-rotating frame. A BEC (gray circle) is formed in an ideal harmonic trap ($\omega_x = \omega_y \equiv \omega_{\perp}$) at the trap center. **First Split:** laser pulses are used to split the BEC into two clouds that move at speed v_B along the $+y$ axis (cloud 1) and the $-y$ axis (cloud 2), respectively. **Second Split:** At time $t = t_1$ cloud 1 at the top is split into clouds 11 and 12. Cloud 11 has a $+v_B \hat{\mathbf{y}}$ added to its velocity by the split while cloud 12 has $-v_B \hat{\mathbf{y}}$ added. These clouds move around a circular orbit in opposite directions. Cloud 2 at the bottom is split into clouds 21 and 22 that also orbit oppositely. **Final Split:** both of these cloud pairs are allowed to execute one orbit and, at time $t = t_2$, when each pair of clouds re-overlaps, they are split in the same way as the Second Split. Each re-overlapped pair is split into four clouds: two overlapping clouds that are nearly motionless and two that continue orbiting in opposite directions. Thus, the (11,12) cloud pair form one Sagnac interferometer, which we will call the “plus” (+) Sagnac interferometer and the (21,22) cloud pair forms the “minus” (−) Sagnac interferometer.

The two clouds fly apart until, at time $t = t_1$, they are each split along the x axis to the new clouds, by another pair of laser pulses (Second Split). The time t_1 is one quarter of the horizontal trap period where the two clouds would be stopped in a purely harmonic trap. The Second Split creates two pairs of counter-orbiting clouds. Each pair of clouds implements a Sagnac interferometer. We will call the pair of clouds shown at the top in the figure (labeled 11 and 12) the plus (+) interferometer and the bottom pair (labeled 21 and 22) the minus (−) interferometer.

These clouds are allowed to orbit until time $t = t_2$ at which time the x -axis splitting lasers are applied again (Final Split). If the potential were purely harmonic, the time elapsed since time t_1 would be one horizontal trap period. As we shall see below the optimal value for the time $t_2 - t_1$ should be the time of maximum overlap of the orbiting clouds which will differ from the trap period due to anharmonic terms present in the external potential. For each Sagnac interferometer this produces a pair of overlapped clouds of stopped atoms plus two clouds that continue orbiting. An image of the system is taken at this point.

Analysis of this image enables the fraction of stopped atoms, the ratio of stopped atoms to total number of atoms in each interferometer, to be measured for this instance of the AI sequence. The result is a stopped-atom fraction for the top interferometer, S_+ , and a fraction for the bottom interferometer, S_- . Due to mechanical vibrations and other technical noise sources, the phase measured in each single interferometer is noisy. However, the phase difference between the two interferometers is stable, and nominally given by the Sagnac expression. To extract the Sagnac phase, the AI sequence is repeated a number of times under the same conditions, and the values of S_+ are plotted versus S_- . These data points are fitted to an ellipse from which can be extracted the differential phase difference:

$$\Delta\Phi = \Delta\Phi_+ - \Delta\Phi_- \quad (8)$$

where $\Delta\Phi_{\pm}$ is the phase difference between the two stopped-atom clouds in the \pm Sagnac interferometers, respectively. In this way, common-mode noise sources are subtracted out while the Sagnac phase contributions add since they affect the two interferometers oppositely. Our model accounts for Sagnac effects and for interaction and finite-size effects. There are no noise sources in the model so we can determine $\Delta\Phi_{\pm}$ for each interferometer separately with no need for ellipse fitting.

Analysis of the TOP (time-averaged orbiting potential) trap used in the experiment carried out by the Virginia group indicated that there were anharmonic terms present in the potential that could impact the performance of the interferometer [67]. The potential experienced by the condensate atoms can be expressed as follows:

$$V(\mathbf{r}) = M\omega_0^2 \left[\frac{1}{2}\rho^2 + \frac{1}{2}\lambda^2 z^2 + \frac{1}{3}az^3 + \frac{1}{2}b\rho^2 z + \frac{1}{4}c\rho^4 + \frac{1}{4}fz^4 + \frac{1}{2}h\rho^2 z^2 \right], \quad (9)$$

where m is the mass of a condensate atom and ω_0 is given by

$$\omega_0 = \left(\frac{7}{64} \frac{\mu}{M} \frac{(B'_1)^2}{B_0} \right)^{1/2}.$$

and where μ is the magnetic dipole moment of the trapped state, B_0 is the TOP trap bias field and B'_1 is the gradient of the quadrupole magnetic field. The case of a trap produced by spatially uniform bias and gradient fields was considered in [67], where the coefficients appearing in the potential were calculated in terms of $\kappa \equiv B'_1/B_0$ as follows:

$$\lambda^2 = \frac{8}{7} \quad a = \frac{6}{7}\kappa \quad b = \frac{9}{14}\kappa \quad c = -\frac{237}{3584}\kappa^2 \quad f = \frac{17}{28}\kappa^2 \quad h = \frac{93}{224}\kappa^2. \quad (10)$$

4. Model Equations of Motion for a Power-Law Potential

In order to simulate the dual-Sagnac interferometer sequence described above and account for anharmonic terms in the external potential we will derive the variational

equations of motion for a 3D power-law potential. We will assume that the potential has the form

$$V_{\text{ext}}(\mathbf{r}) \equiv \sum_{k=1}^{N_{\text{terms}}} C_{p_x(k), p_y(k), p_z(k)} x^{p_x(k)} y^{p_y(k)} z^{p_z(k)}. \quad (11)$$

We consider the case where the atoms move over a length scale that is small compared to the distance at which anharmonicities become large, so that the impact of terms in (11) decreases as the powers increase. If we include all triples, (p_x, p_y, p_z) , of powers such that

$$p_x + p_y + p_z \leq N_{\text{max}} \quad \text{then} \quad N_{\text{terms}} = \frac{1}{6} N_{\text{max}} (N_{\text{max}}^2 + 6N_{\text{max}} + 11) \quad (12)$$

excluding the term where all powers are zero. The analysis in [16] considered anharmonic terms up to fourth power, so we take $N_{\text{max}} = 4$ and $N_{\text{terms}} = 34$.

The equations of motion for the general power-law potential are derived in Appendix A. The result is

$$\ddot{x}_j = 2\Omega_z \dot{y}_j + \Omega_z^2 x_j - \frac{1}{M} \frac{\partial U_{\text{ext}}^{(3D)}}{\partial x_j} - \frac{1}{M} F_{jx}(\mathbf{x}, \mathbf{w}), \quad (13a)$$

$$\ddot{y}_j = -2\Omega_z \dot{x}_j + \Omega_z^2 y_j - \frac{1}{M} \frac{\partial U_{\text{ext}}^{(3D)}}{\partial y_j} - \frac{1}{M} F_{jy}(\mathbf{x}, \mathbf{w}), \quad (13b)$$

$$\ddot{z}_j = -\frac{1}{M} \frac{\partial U_{\text{ext}}^{(3D)}}{\partial z_j} - \frac{1}{M} F_{jz}(\mathbf{x}, \mathbf{w}), \quad (13c)$$

$$\ddot{w}_{j\eta} = \frac{\hbar^2}{M^2} w_{j\eta}^{-3} - \frac{2}{M} \frac{\partial U_{\text{ext}}^{(3D)}}{\partial w_{j\eta}} + \frac{gN}{(2\pi)^{3/2} N_c M} \left(\frac{1}{w_{jx} w_{jy} w_{jz} w_{j\eta}} \right) - \frac{1}{M} W_{j\eta}(\mathbf{x}, \mathbf{w}), \quad (13d)$$

$$\eta = x, y, z \quad j = 1, \dots, N_c$$

The full expression for $U_{\text{ext}}^{(3D)}(\mathbf{x}, \mathbf{w})$ for the general power-law potential is given by Equation (A4). Expressions for $F_{j\eta}(\mathbf{x}, \mathbf{w})$ and $W_{j\eta}(\mathbf{x}, \mathbf{w})$ were derived in Ref. [60] and are given in full in Appendix B.

These equations of motion apply to a system of N_c condensate clouds that are subjected to the power-law potential defined above. The terms $F_{j\eta}(\mathbf{x}, \mathbf{w})$ in the cloud-center equations of motion represent interaction forces exerted on cloud j when it overlaps one or more of the other clouds. The third term on the right-hand-side of Equation (13d) accounts for the effects of self interaction of cloud j . They cause cloud j to expand or contract during its evolution. The terms $W_{j\eta}(\mathbf{x}, \mathbf{w})$ account for the evolution of the widths of cloud j when it overlaps other clouds.

It is worth noting that the $F_{j\eta}$ and $W_{j\eta}$ terms are negligible when clouds are not overlapping. The size of these terms decays as the exponential of the square of the center separation distance between the two overlapping clouds. This can be seen from their expressions given in Equations (A7) and (A9) of Appendix B.

Virginia Trap Potential Equations of Motion

We can derive the equations of motion for the particular case of the anharmonic potential present in the Virginia experiment described earlier and given in Equation (9). This potential can be written in the form of the general power-law potential defined in Equation (11)

$$\begin{aligned} V_{\text{ext}}(\mathbf{r}) = & C_{200} x^2 y^0 z^0 + C_{020} x^0 y^2 z^0 + C_{002} x^0 y^0 z^2 + C_{201} x^2 y^0 z^1 + C_{021} x^0 y^2 z^1 + C_{003} x^0 y^0 z^3 \\ & + C_{400} x^4 y^0 z^0 + C_{220} x^2 y^2 z^0 + C_{040} x^0 y^4 z^0 + C_{202} x^2 y^0 z^2 + C_{022} x^0 y^2 z^2 + C_{004} x^0 y^0 z^4. \end{aligned} \quad (14)$$

Comparing with Equation (9) the coefficients are given by

$$C_{200} = C_{020} = C_{002} / \lambda^2 = \frac{1}{2} M \omega_0^2, \quad C_{201} = C_{021} = \frac{1}{2} M \omega_0^2 b, \quad C_{003} = \frac{1}{3} M \omega_0^2 a$$

$$C_{400} = C_{040} = C_{220}/2 = \frac{1}{4}M\omega_0^2c, \quad C_{202} = C_{022} = \frac{1}{2}M\omega_0^2h, \quad C_{004} = \frac{1}{4}M\omega_0^2f$$

We can find the variational potential, $U_{\text{ext}}^{(3D)}$, corresponding to the anharmonic potential given above in Equation (14) by using Equation (A3) for the general power-law potential. Each term in V_{ext} has a corresponding term in $U_{\text{ext}}^{(3D)}$. The term in $U_{\text{ext}}^{(3D)}$ corresponding to $C_{\alpha\beta\gamma}x^\alpha y^\beta z^\gamma$ in V_{ext} is $C_{\alpha\beta\gamma}J_\alpha(x_j, w_{jx})J_\beta(y_j, w_{jy})J_\gamma(z_j, w_{jz})$. Since the maximum power is 4, we only need the following $J_n(\eta, w)$: $J_0 = 1$, $J_1 = \eta$, $J_2 = \eta^2 + \frac{1}{2}w^2$, $J_3 = \eta^3 + \frac{3}{2}\eta w^2$, and $J_4 = \eta^4 + 3\eta^2 w^2 + \frac{3}{4}w^4$.

This process yields the specific form of $U_{\text{ext}}^{(3D)}$ for the Virginia potential. The result is

$$\begin{aligned} U_{\text{ext}}^{(3D)}(\mathbf{x}, \mathbf{w}) = & \sum_{j=1}^{N_{\text{terms}}} \left(C_{200}(x_j^2 + \frac{1}{2}w_{jx}^2) + C_{020}(y_j^2 + \frac{1}{2}w_{jy}^2) + C_{002}(z_j^2 + \frac{1}{2}w_{jz}^2) \right. \\ & + C_{201}(x_j^2 + \frac{1}{2}w_{jx}^2)z_j + C_{021}(y_j^2 + \frac{1}{2}w_{jy}^2)z_j + C_{003}(z_j^3 + \frac{3}{2}z_j w_{jz}^2) \\ & + C_{400}(x_j^4 + 3x_j^2 w_{jx}^2 + \frac{3}{4}w_{jx}^4) + C_{220}(x_j^2 + \frac{1}{2}w_{jx}^2)(y_j^2 + \frac{1}{2}w_{jy}^2) \\ & + C_{040}(y_j^4 + 3y_j^2 w_{jy}^2 + \frac{3}{4}w_{jy}^4) + C_{202}(x_j^2 + \frac{1}{2}w_{jx}^2)(z_j^2 + \frac{1}{2}w_{jz}^2) \\ & \left. + C_{022}(y_j^2 + \frac{1}{2}w_{jy}^2)(z_j^2 + \frac{1}{2}w_{jz}^2) + C_{004}(z_j^4 + 3z_j^2 w_{jz}^2 + \frac{3}{4}w_{jz}^4) \right). \end{aligned} \quad (15)$$

This potential can be used to write down the equations of motion for the specific case of the Virginia trap potential.

The center-coordinate equations of motion for the potential have the following form:

$$\begin{aligned} \ddot{x}_j + (\omega_0^2 - \Omega_z^2)x_j &= +2\Omega_z \dot{y}_j - \omega_0^2 b z_j x_j - \omega_0^2 c(x_j^2 + \frac{3}{2}w_{jx}^2)x_j - \omega_0^2 c(y_j^2 + \frac{1}{2}w_{jy}^2)x_j \\ &- \omega_0^2 h(z_j^2 + \frac{1}{2}w_{jz}^2)x_j - \frac{1}{M}F_{jx}(\mathbf{x}, \mathbf{w}) \\ \ddot{y}_j + (\omega_0^2 - \Omega_z^2)y_j &= -2\Omega_z \dot{x}_j - \omega_0^2 b z_j y_j - \omega_0^2 c(y_j^2 + \frac{3}{2}w_{jy}^2)y_j - \omega_0^2 c(x_j^2 + \frac{1}{2}w_{jx}^2)y_j \\ &- \omega_0^2 h(z_j^2 + \frac{1}{2}w_{jz}^2)y_j - \frac{1}{M}F_{jy}(\mathbf{x}, \mathbf{w}) \\ \ddot{z}_j + \lambda^2 \omega_0^2 z_j &= -\frac{1}{2}\omega_0^2 b(x_j^2 + \frac{1}{2}w_{jx}^2) - \frac{1}{2}\omega_0^2 b(y_j^2 + \frac{1}{2}w_{jy}^2) - \omega_0^2 a(z_j^2 + \frac{1}{2}w_{jz}^2) \\ &- \omega_0^2 h(x_j^2 + \frac{1}{2}w_{jx}^2)z_j - \omega_0^2 h(y_j^2 + \frac{1}{2}w_{jy}^2)z_j - \omega_0^2 f(z_j^2 + \frac{3}{2}w_{jz}^2)z_j - \frac{1}{M}F_{jz}(\mathbf{x}, \mathbf{w}) \\ j &= 1, \dots, N_c \end{aligned} \quad (16)$$

The EOMs for the widths are

$$\begin{aligned} \ddot{w}_{jx} + \omega_0^2 w_{jx} &= \frac{\hbar^2}{M^2} w_{jx}^{-3} + \frac{gN}{(2\pi)^{3/2} N_c M} \left(\frac{1}{w_{jx} w_{jy} w_{jz} w_{jx}} \right) - \omega_0^2 b z_j w_{jx} - 3\omega_0^2 c(x_j^2 + \frac{1}{2}w_{jx}^2)w_{jx} \\ &- \omega_0^2 c(y_j^2 + \frac{1}{2}w_{jy}^2)w_{jx} - \omega_0^2 h(z_j^2 + \frac{1}{2}w_{jz}^2)w_{jx} - \frac{1}{M}W_{jx}(\mathbf{x}, \mathbf{w}) \\ \ddot{w}_{jy} + \omega_0^2 w_{jy} &= \frac{\hbar^2}{M^2} w_{jy}^{-3} + \frac{gN}{(2\pi)^{3/2} N_c M} \left(\frac{1}{w_{jx} w_{jy} w_{jz} w_{jy}} \right) - \omega_0^2 b z_j w_{jy} - 3\omega_0^2 c(y_j^2 + \frac{1}{2}w_{jy}^2)w_{jy} \\ &- \omega_0^2 c(x_j^2 + \frac{1}{2}w_{jx}^2)w_{jy} - \omega_0^2 h(z_j^2 + \frac{1}{2}w_{jz}^2)w_{jy} - \frac{1}{M}W_{jy}(\mathbf{x}, \mathbf{w}) \\ \ddot{w}_{jz} + \lambda^2 \omega_0^2 w_{jz} &= \frac{\hbar^2}{M^2} w_{jz}^{-3} + \frac{gN}{(2\pi)^{3/2} N_c M} \left(\frac{1}{w_{jx} w_{jy} w_{jz} w_{jz}} \right) - 2\omega_0^2 a z_j w_{jz} - 3\omega_0^2 f(z_j^2 + \frac{1}{2}w_{jz}^2)w_{jz} \\ &- \omega_0^2 h(x_j^2 + \frac{1}{2}w_{jx}^2)w_{jz} - \omega_0^2 h(y_j^2 + \frac{1}{2}w_{jy}^2)w_{jz} - \frac{1}{M}W_{jz}(\mathbf{x}, \mathbf{w}) \\ j &= 1, \dots, N_c \end{aligned} \quad (17)$$

We again note here that the terms $F_{j\eta}(\mathbf{x}, \mathbf{w})$ and $W_{j\eta}(\mathbf{x}, \mathbf{w})$ account for interactions between different clouds and couple the widths and center coordinates of cloud j to the widths and centers of all the other clouds. These terms are negligible unless cloud j has a spatial overlap with another cloud.

5. Computing the Stopped-Atom Fraction within the Variational Model

Our model is applied to the Virginia interferometer sequence by first finding stationary values of the center coordinates and x, y, z widths in the one-cloud ($N_c = 1$) version of the equations given in Equation (5a–e) to model the initial condensate. The two-cloud ($N_c = 2$) version of the model is used to simulate the trajectories after the First Split. The one-cloud-model values for the center coordinates and widths plus their y velocities modified by the kick imparted by the lasers in the First Split are used as initial conditions for the two-cloud model. Following the protocol, after one-quarter of the trap period, the Second Split is applied and the four-cloud version ($N_c = 4$) of the equations is used to simulate the system evolution for one full trap period. The final values of the centers and widths and their derivatives (modified to include the laser kick applied in the Second Split) are used as the initial conditions for the four-cloud model.

The variational trial wave function given by Equation (2), at time $t = t_2$ (four-cloud model) just before the Final Split, can be written as

$$\begin{aligned}\Psi(\mathbf{r}, t_2) &= \frac{1}{2} \left(A_{11}(t) e^{g_{11}(\mathbf{r}, t_2)} + A_{12}(t) e^{g_{12}(\mathbf{r}, t_2)} + A_{21}(t) e^{g_{21}(\mathbf{r}, t_2)} + A_{22}(t) e^{g_{22}(\mathbf{r}, t_2)} \right) \\ &\equiv \psi_{11}(\mathbf{r}, t_2) + \psi_{12}(\mathbf{r}, t_2) + \psi_{21}(\mathbf{r}, t_2) + \psi_{22}(\mathbf{r}, t_2).\end{aligned}$$

where

$$g_{ij}(\mathbf{r}, t_2) \equiv \sum_{\eta=x,y,z} \left(-\frac{(\eta - \eta_{ij}(t_2))^2}{2(w_{ij\eta}(t_2))^2} + i(\epsilon_{ij\eta}(t_2)\eta + \beta_{ij}(t_2)\eta^2) \right), \quad ij = 11, 12, 21, 22$$

and

$$\begin{aligned}\epsilon_{ijx}(t_2) &\equiv \frac{M}{\hbar} (\dot{x}_{ij}(t_2) - \Omega_z y_{ij}(t_2)) - 2\beta_{ijx}(t_2) x_{ij}(t_2) \\ \epsilon_{ijy}(t_2) &\equiv \frac{M}{\hbar} (\dot{y}_{ij}(t_2) + \Omega_z x_{ij}(t_2)) - 2\beta_{ijy}(t_2) y_{ij}(t_2) \\ \epsilon_{ijz}(t_2) &\equiv \frac{M}{\hbar} \dot{z}_{ij}(t_2) - 2\beta_{ijz}(t_2) z_{ij}(t_2).\end{aligned}$$

The first two terms, ψ_{11} and ψ_{12} , represent the plus (top) Sagnac interferometer shown in Figure 1 while the last two terms, ψ_{21} and ψ_{22} , represent the minus (bottom) Sagnac interferometer. We note that clouds belonging to different interferometers at time $t = t_2$ have no spatial overlap, so that any product of a plus interferometer cloud and a minus cloud will be strictly zero.

The final split has the effect of stopping half of cloud ij and leaving the other half alone ($ij = 11, 12, 21$, or 22). Since, at $t = t_2$, the clouds 11 and 21 move nearly along $+x$ and clouds 12 and 22 move nearly along $-x$, after the final split we have

$$\psi_{ij}(\mathbf{r}, t_2) \rightarrow \frac{1}{\sqrt{2}} \left(\psi_{ij}(\mathbf{r}, t_2) + \psi_{ij}(\mathbf{r}, t_2) e^{-i\lambda_{ij} M v_{Bx} x / \hbar} \right)$$

where $\lambda_{11} = \lambda_{21} = -\lambda_{12} = -\lambda_{22} = 1$ and where the term with the exponential is the stopped cloud. Since there is no spatial overlap between any linear combination of the 11 and 12 clouds with any linear combination of the 21 and 22 clouds, we may treat them separately. Each constitutes a separate Sagnac interferometer.

The quantities that can be determined from the image data generated in the Virginia experiment are the ratios, S_{\pm} , of the number of stopped atoms to the total number of atoms in the two Sagnac interferometers. We can compute this from the variational wave function just at the moment of the final split as the probability of being in the zero-momentum state. Since the clouds of the two interferometers have no spatial overlap, the fraction of stopped atoms in each interferometer can be written as

$$S_{+} = \int d^3r \left| \psi_{11}(\mathbf{r}, t_2) e^{-iMv_{Bx}x/\hbar} + \psi_{21}(\mathbf{r}, t_2) e^{+iMv_{Bx}x/\hbar} \right|^2$$

and

$$S_- = \int d^3r \left| \psi_{21}(\mathbf{r}, t_2) e^{-iMv_B x/\hbar} + \psi_{22}(\mathbf{r}, t_2) e^{+iMv_B x/\hbar} \right|^2$$

We can express S_{\pm} in terms of the variational parameters by inserting the expression for the trial wave function into the above integrals and carrying out the integration. The result is

$$\begin{aligned} S_+ &= \frac{1}{2} + \frac{1}{2} \text{Re} \left\{ M(x_{11}(t_2), w_{11x}(t_2), \epsilon_{11x}(t_2), \beta_{11x}(t_2), x_{12}(t_2), w_{12x}(t_2), \epsilon_{12x}(t_2) + \frac{Mv_B}{\hbar}, \beta_{12x}(t_2)) \right. \\ &\times M(y_{11}(t_2), w_{11y}(t_2), \epsilon_{11y}(t_2), \beta_{11y}(t_2), y_{12}(t_2), w_{12y}(t_2), \epsilon_{12y}(t_2), \beta_{12y}(t_2)) \\ &\times M(z_{11}(t_2), w_{11z}(t_2), \epsilon_{11z}(t_2), \beta_{11z}(t_2), z_{12}(t_2), w_{12z}(t_2), \epsilon_{12z}(t_2), \beta_{12z}(t_2)) \left. \right\} \end{aligned} \quad (18)$$

$$\begin{aligned} S_- &= \frac{1}{2} + \frac{1}{2} \text{Re} \left\{ M(x_{21}(t_2), w_{21x}(t_2), \epsilon_{21x}(t_2), \beta_{21x}(t_2), x_{22}(t_2), w_{22x}(t_2), \epsilon_{22x}(t_2) + \frac{Mv_B}{\hbar}, \beta_{22x}(t_2)) \right. \\ &\times M(y_{21}(t_2), w_{21y}(t_2), \epsilon_{21y}(t_2), \beta_{21y}(t_2), y_{22}(t_2), w_{22y}(t_2), \epsilon_{22y}(t_2), \beta_{22y}(t_2)) \\ &\times M(z_{21}(t_2), w_{21z}(t_2), \epsilon_{21z}(t_2), \beta_{21z}(t_2), z_{22}(t_2), w_{22z}(t_2), \epsilon_{22z}(t_2), \beta_{22z}(t_2)) \left. \right\} \end{aligned} \quad (19)$$

where

$$M(x_1, w_1, \epsilon_1, \beta_1, x_2, w_2, \epsilon_2, \beta_2) = \frac{\exp \left\{ \left(\frac{x_1}{2w_1^2} + \frac{x_2}{2w_2^2} + \frac{1}{2} i(\epsilon_2 - \epsilon_1) \right)^2 - \left(\frac{x_1^2}{2w_1^2} + \frac{x_2^2}{2w_2^2} \right) \right\}}{\left(\frac{w_2}{2w_1} + \frac{w_1}{2w_2} - i(\beta_2 - \beta_1)w_1w_2 \right)^{1/2}}. \quad (20)$$

These expressions enable us to compute S_{\pm} in terms of the values of the variational parameters just before the Final Split.

6. Approximate Expressions for the Stopped-Atom Fraction

6.1. Stopped-Atom Fraction for Zero Rotation Speed

We can derive an approximate expression for S_+ for the case of the Virginia trap potential, where cloud–cloud interactions are neglected, and where the rotating-frame speed is zero ($\Omega_z = 0$). We can simplify the formula for $S_+(\Omega_z)$ Equation (18) at $\Omega_z = 0$ by taking advantage of certain symmetries in the solution of the model equations for the zero-rotation case. These are that the x and \dot{x} of clouds 11 and 12 are negatives of each other, the y and \dot{y} of these clouds are the same, and the z and \dot{z} of the clouds are the same at all times. Quantitatively we have

$$\begin{aligned} x_{11}(t) &\equiv x_1(t), & x_{12}(t) &\equiv x_2(t), & x_1(t) &= -x_2(t), & \dot{x}_1(t) &= -\dot{x}_2(t) \\ y_{11}(t) &= y_{12}(t), & \dot{y}_{11}(t) &= \dot{y}_{12}(t), & z_{11}(t) &= z_{12}(t), & \dot{z}_{11}(t) &= \dot{z}_{12}(t), \end{aligned}$$

Furthermore all of the x and y widths and their dots for both clouds are the same at all times:

$$\begin{aligned} w_{11x}(t) &= w_{12x}(t) = w_{11y}(t) = w_{12y}(t) \equiv w_{\perp}(t) \\ \dot{w}_{11x}(t) &= \dot{w}_{12x}(t) = \dot{w}_{11y}(t) = \dot{w}_{12y}(t) \equiv \dot{w}_{\perp}(t) \end{aligned}$$

Additionally, the z widths and dot widths of the two clouds are equal

$$w_{11z}(t) = w_{12z}(t) \equiv w_z(t), \quad \text{and} \quad \dot{w}_{11z}(t) = \dot{w}_{12z}(t) \equiv \dot{w}_z(t)$$

These symmetries greatly simplify the expression for $S_+(0)$.

The simplified expression is

$$S_+(0) = \frac{1}{2} + \frac{1}{2} \exp \left\{ - \left(\frac{M}{\hbar} \right)^2 \left[\frac{1}{2} (2v_B - (\dot{x}_1 - \dot{x}_2))w_{\perp} + (x_1 - x_2)\dot{w}_{\perp} \right]^2 - \left(\frac{x_1^2}{2w_{\perp}^2} + \frac{x_2^2}{2w_{\perp}^2} \right) \right\} \quad (21)$$

where $x_1, x_2, \dot{x}_1, \dot{x}_2, w_\perp$, and \dot{w}_\perp are all evaluated at time $t = t_2$, the moment of the final split. This result provides insight into the model-predicted physical mechanisms that affect the fraction of stopped atoms when the counter-orbiting clouds recombine just before the final split.

The exponential in Equation (21) contains two terms. The first term, shown enclosed by square brackets, is due to the relative velocity of the two clouds. The second term, shown in parenthesis, is due to the finite widths of the two clouds compared with the separation of their center coordinates.

The relative velocity term has two contributions. The first term inside the square brackets is the difference between the relative velocity of the center coordinates of the two clouds, $(\dot{x}_1 - \dot{x}_2)$ and their initial relative velocity at the second split ($2v_B$). The second contribution to the relative velocity is due to the expansion or contraction of the two clouds. Even though the expansion and contraction of the two clouds is the same, if their centers are offset, then there will be a relative velocity due to the time rate of change of the width, \dot{w}_\perp .

The finite-width term decreases the fraction of stopped atoms the further apart the two clouds are and the narrower their widths are relative to their separation. Thus, the closer together and wider the clouds are, the larger the fraction of stopped atoms. This is an entirely intuitive result since both decreased separation and larger widths tend to maximize overlap and thus increase the possibility of interference.

6.2. Exact Stopped-Atom Fraction for Non-Interacting Clouds in a Harmonic Potential

The variational equations of motion applied to the Virginia experiment, found in Equations (16) and (17), for the case of a harmonic potential and where cloud–cloud interactions are neglected have the form

$$\begin{aligned} \ddot{x}_j + (\omega_0^2 - \Omega_z^2)x_j &= +2\Omega_z\dot{y}_j \\ \ddot{y}_j + (\omega_0^2 - \Omega_z^2)y_j &= -2\Omega_z\dot{x}_j \\ \ddot{z}_j + \lambda^2\omega_0^2z_j &= 0 \\ \ddot{w}_{jx} + \omega_0^2w_{jx} &= \frac{\hbar^2}{M^2}w_{jx}^{-3} + \frac{gN}{(2\pi)^{3/2}N_cM} \left(\frac{1}{w_{jx}w_{jy}w_{jz}w_{jx}} \right) \\ \ddot{w}_{jy} + \omega_0^2w_{jy} &= \frac{\hbar^2}{M^2}w_{jy}^{-3} + \frac{gN}{(2\pi)^{3/2}N_cM} \left(\frac{1}{w_{jx}w_{jy}w_{jz}w_{jy}} \right) \\ \ddot{w}_{jz} + \lambda^2\omega_0^2w_{jz} &= \frac{\hbar^2}{M^2}w_{jz}^{-3} + \frac{gN}{(2\pi)^{3/2}N_cM} \left(\frac{1}{w_{jx}w_{jy}w_{jz}w_{jz}} \right) \\ j &= 1, \dots, N_c. \end{aligned} \quad (22)$$

The equations for the center coordinates of each cloud form a closed set and can be solved exactly. The width equations must be solved numerically, but exhibit a clear symmetry in that the equations for $w_{jx}(t)$ and $w_{jy}(t)$ are the same. When the initial conditions for these widths are the same (as is the case when applying the one, two, and four-cloud models to the Virginia AI sequence) the solutions $w_{jx}(t)$ and $w_{jy}(t)$ will be identical. Note that the evolution of the widths do not depend on the speed, Ω_z , of the rotating frame, as this does not appear in the width equations of motion.

Using the analytical solutions of the cloud-center equations of motion and the symmetries of the solutions of the width equations of motion, we can follow the steps of the Virginia AI sequence to obtain an analytical expression for $S_+(\Omega_z)$. The result is

$$S_+(\Omega_z) = \frac{1}{2} + \frac{1}{2} \exp \left\{ - \left(\frac{2Mv_B w_\perp}{\hbar} \right)^2 \sin^2 \left(\pi \frac{\Omega_z}{\omega_0} \right) \right\} \cos \left\{ \left(\frac{2Mv_B^2}{\hbar\omega_0} \right) \left(\sin \left(\frac{5\pi}{2} \frac{\Omega_z}{\omega_0} \right) - \sin \left(\frac{\pi}{2} \frac{\Omega_z}{\omega_0} \right) \right) \right\} \quad (23)$$

and the expression for $S_-(\Omega_z)$ is identical. In the above, $w_\perp = w_{jx}(t_2) = w_{jy}(t_2)$ is the transverse width of the condensate at the moment of the Final Split.

In the limit where the rotation speed is much smaller than the trap frequency, $\Omega_z \ll \omega_0$, this approximates to

$$S_+(\Omega_z) = \frac{1}{2} + \frac{1}{2} \exp \left\{ - \left(\frac{2\pi M v_B w_\perp}{\hbar \omega_0} \right)^2 \Omega_z^2 \right\} \cos \left\{ \left(\frac{4M\pi(v_B/\omega_0)^2 \Omega_z}{\hbar} \right) \right\} \quad (24)$$

For a purely harmonic potential, the radius of the circular orbit followed by the condensate clouds is given by $R = v_B/\omega_0$ so that the area of this orbit (and thus the interferometer area) is $A = \pi R^2 = \pi(v_B/\omega_0)^2$. This enables us to recognize the argument of the cosine above as the Sagnac phase for a single interferometer:

$$\Phi_S = \frac{4M\pi(v_B/\omega_0)^2 \Omega_z}{\hbar} = \frac{4MA\Omega_z}{\hbar}.$$

The expression for $S_+(\Omega_z)$ in Equation (24) provides guidance for simulations where inter-cloud interactions and anharmonic terms in the potential are included.

7. Interaction and Anharmonic Effect Study

We studied the effects of interactions and the presence of anharmonic terms in the potential by computing the dependence of S_+ on the true rotation speed Ω_z by simulating the interferometer experiment for various conditions. These conditions included harmonic or anharmonic potential, cloud–cloud interactions on or off, and number of condensate atoms. These numbers were $N = 1 \times 10^4, 1 \times 10^5, 2 \times 10^5, 3 \times 10^5, 4 \times 10^5, 5 \times 10^5, 6 \times 10^5, 7 \times 10^5, 8 \times 10^5, 9 \times 10^5, 1 \times 10^6, 2 \times 10^6$ atoms. In all there were 48 sets of combinations of harmonic or anharmonic potential, cloud–cloud interactions off or on, and number of condensate atoms. For each of these 48 combinations of potential, interactions, and condensate number, we simulated the interferometer experiment at 26 different input rotation speeds at equal intervals ranging from zero up to 125 times the Earth’s rotation speed. The values of S_+ were then plotted versus Ω_z for each case. All other parameter values were taken from the original Virginia experiment.

We fitted the S_+ vs. Ω_z plots to a function, which has the same dependence on Ω_z as the expression for S_+ in Equation (24) for the case of a harmonic potential and no cloud–cloud interactions. The fit function was

$$S_+(a, b, c, \Omega_z) = \frac{1}{2} + a e^{-b\Omega_z^2} \cos(2\pi c\Omega_z). \quad (25)$$

The fits were performed for data where the rotation speeds were expressed in Hertz. Thus, the b parameter is measured in seconds squared and the c parameter is measured in seconds.

We can use Equation (21) to find an approximate expression for the a parameter. Note that, when $\Omega_z = 0$, the above expression becomes $S_+(0) = 1/2 + a$. Comparing this with Equation (21) gives an approximate formula for a

$$a \approx \frac{1}{2} \exp \left\{ - \left(\frac{M}{\hbar} \right)^2 \left[\frac{1}{2} (2v_B - (\dot{x}_1 - \dot{x}_2)) w_\perp + (x_1 - x_2) \dot{w}_\perp \right]^2 - \left(\frac{x_1^2}{2w_\perp^2} + \frac{x_2^2}{2w_\perp^2} \right) \right\}. \quad (26)$$

Comparing the fit function with Equation (24) gives an approximate expression for the b parameter

$$b \approx \left(\frac{4\pi^2 M v_B}{\hbar \omega_0} \right)^2 w_\perp^2 \quad (27)$$

where we note that this equation gives the value of b when the Ω_z appearing in the exponential is measured in Hz.

It is clear from these expressions that the width of the clouds, w_\perp , and to a lesser extent the width velocity, \dot{w}_\perp , at the final split have a major effect on the value of S_+ . The cloud

widths are the direct result of atom–atom interactions and Figures 2 and 3 show that this causes the stopped-atom signal to decay as the rotation speed increases. This figure also shows that the presence of anharmonic terms in the potential can dramatically reduce the range of the stopped-atom fraction signal.

The c parameter can be approximated by assuming that the quantity appearing in the cosine term is just the Sagnac phase. Since the full potential including the anharmonic terms has cylindrical symmetry, the z component of the angular momentum of each cloud is conserved. Thus, if Ω_z in the $\cos(2\pi c\Omega_z)$ factor in Equation (25) is measured in Hz, we have

$$\begin{aligned} c &= \frac{1}{\hbar} \int_{t_i}^{t_f} dt (L_{2z}(t) - L_{1z}(t)) = (L_{2z}(t_f) - L_{1z}(t_f)) \int_{t_i}^{t_f} dt \\ c &\approx \left(\frac{M(t_f - t_i)}{\hbar} \right) ((x_2 \dot{y}_2 - y_2 \dot{x}_2) - (x_1 \dot{y}_1 - y_1 \dot{x}_1)). \end{aligned} \quad (28)$$

In the last expression, all quantities are evaluated at time $t = t_2$. It will be instructive to compare the values of a , b , and c given by these approximate formulas with their values determined from the simulation fits.

Plots of S_+ versus Ω_z for $N_{\text{atoms}} = 10,000$ atoms are shown in Figure 2 and for $N_{\text{atoms}} = 1,000,000$ atoms in Figure 3. The four plots found in these figures are for a harmonic potential with cloud–cloud interactions turned off (upper left), harmonic with interactions on (upper right), anharmonic with interactions off (lower left), and anharmonic with interactions on (lower right). These plots also display the values of $S_+(\Omega_z)$ fitted to the function shown in Equation (25). We note that these fits closely follow the simulation data in all cases.

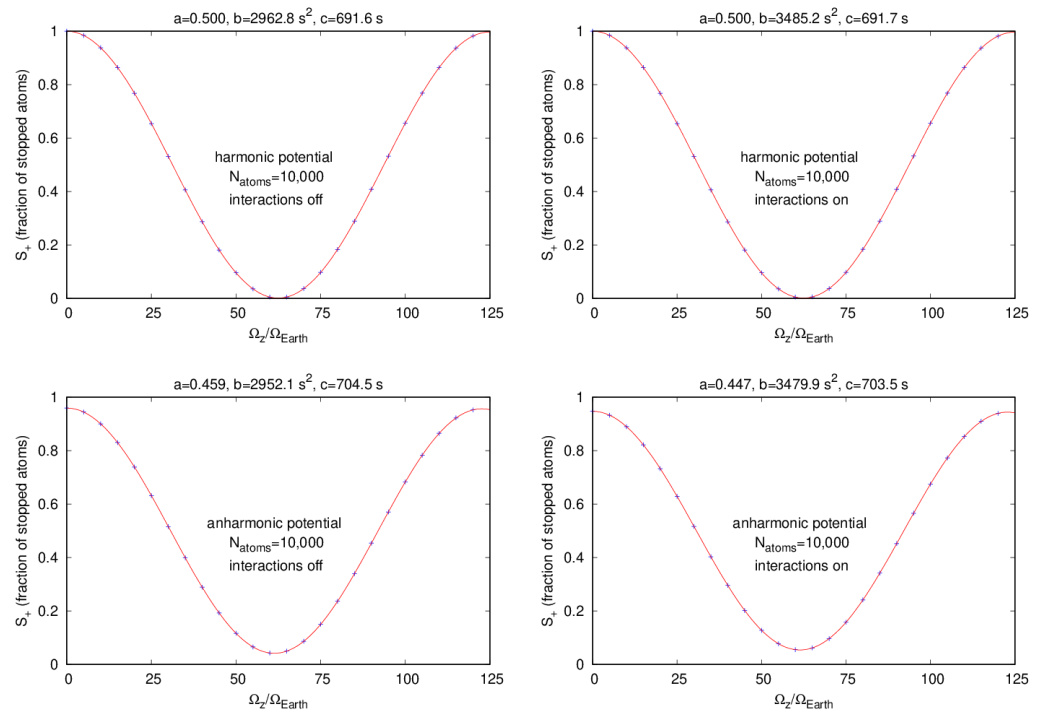


Figure 2. The fraction of stopped atoms, S_+ , vs. rotating frame speed, Ω_z , with $N_{\text{atoms}} = 10,000$ ^{87}Rb atoms for four different cases. **Upper Left:** harmonic potential and cloud–cloud interactions off; **Upper Right:** harmonic potential and interactions on; **Lower Left:** anharmonic potential and interactions off; **Lower Right:** anharmonic potential and interactions on.

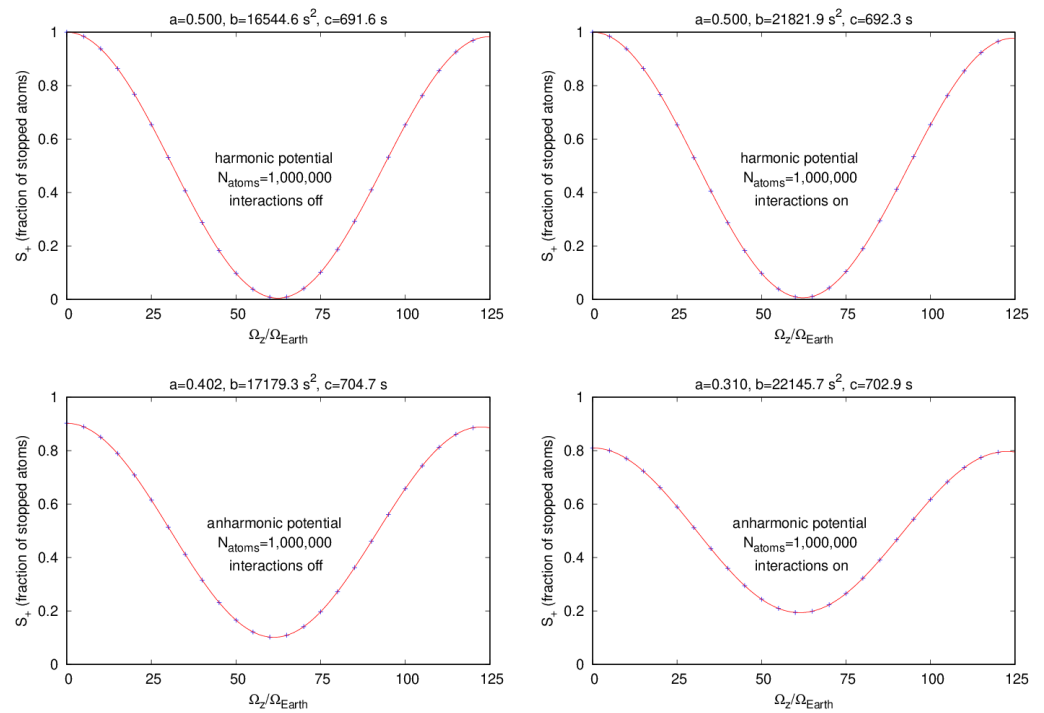


Figure 3. The fraction of stopped atoms, S_+ , vs rotating frame speed, Ω_z , with $N_{\text{atoms}} = 1,000,000$ ^{87}Rb atoms for four different cases. **Upper Left:** harmonic potential and cloud–cloud interactions off; **Upper Right:** harmonic potential and interactions on; **Lower Left:** anharmonic potential and interactions off; **Lower Right:** anharmonic potential and interactions on.

One noticeable feature of these plots is the effect of the anharmonic potential. The maximum and minimum values of S_+ vary between approximately 1 and 0 for the harmonic potential while this variation is reduced for the anharmonic potential. Another smaller effect is that the envelope of the variation of S_+ decreases more rapidly for the anharmonic potential.

The physical mechanisms for these effects can be identified quantitatively by looking at the data found in Tables 1 and 2. Table 1 compares the fitted values of parameters a , b , and c with their values determined from Equations (26)–(28) for six different condensate numbers for the case where cloud–cloud interaction are turn off. The top half of the table contains results for the harmonic potential and the bottom half shows results for the anharmonic potential. Table 2 shows the same comparison when cloud–cloud interactions are on.

The first thing to note is that the approximate formulas for a , b , and c do a good job in predicting the fitted values for these parameters. This is the case for all conditions considered. The formula values for a and c differ from the fitted values by well under 1% and the largest difference in these values for b is less than 5%. Thus, these formulas should provide physical insight into the effects of interactions and the anharmonic potential.

One important feature of the comparisons shown in the tables is that the c parameter is insensitive to the number of condensate atoms. Furthermore, because the fit and formula values for c match well, it shows that the argument, $2\pi c\Omega_z$, is the Sagnac phase. The slightly larger values of c for the anharmonic potential occurs because the anharmonic terms cause the cloud trajectories to move out of the xy plane, thus increasing slightly the area of the interferometer over its value for the harmonic potential.

The a parameter fit and formula comparison is particularly good across all conditions. The expression for a in Equation (26) shows that, in order to maximize a at zero rotation speed, the centers of the two clouds must coincide and their relative velocity x components must be $2v_B$ just before the final split. The agreement between fit and formula values for a show that this physical picture for the value of a works for all conditions.

Table 1. Comparison of the fitted values of the parameters, a , b , and c with their values predicted by Equations (26)–(28) when cloud–cloud interactions are turned off. The top half of the table gives results for a harmonic potential and the bottom half for anharmonic potential.

N_{atoms}	a	a	$b \text{ (s}^2\text{)}$	$b \text{ (s}^2\text{)}$	$c \text{ (s)}$	$c \text{ (s)}$
	(Formula)	(Fit)	(Formula)	(Fit)	(Formula)	(Fit)
10,000	0.500	0.500	2962.6	2962.8	691.6	691.6
100,000	0.500	0.500	6733.3	6733.6	691.6	691.6
200,000	0.500	0.500	8787.9	8788.3	691.6	691.6
500,000	0.500	0.500	12,577.9	12,578.5	691.6	691.6
1,000,000	0.500	0.500	16,543.9	16,544.6	691.6	691.6
2,000,000	0.500	0.500	21,789.6	21,790.4	691.6	691.6
10,000	0.459	0.459	3027.2	2952.1	702.9	704.5
100,000	0.450	0.450	6984.8	6913.5	702.9	704.5
200,000	0.441	0.441	9137.4	9072.4	702.9	704.6
500,000	0.422	0.422	13,101.1	13,039.0	702.9	704.6
1,000,000	0.402	0.402	17,244.1	17,179.3	702.9	704.7
2,000,000	0.376	0.376	22,720.7	22,648.1	703.0	704.7

Table 2. Comparison of the fitted values of the parameters, a , b , and c with their values predicted by Equations (26)–(28) when cloud–cloud interactions are turned on. The top half of the table gives results for a harmonic potential and the bottom half for anharmonic potential.

N_{atoms}	a	a	$b \text{ (s}^2\text{)}$	$b \text{ (s}^2\text{)}$	$c \text{ (s)}$	$c \text{ (s)}$
	(Formula)	(Fit)	(Formula)	(Fit)	(Formula)	(Fit)
10,000	0.500	0.500	3475.6	3485.2	691.7	691.7
100,000	0.500	0.500	8499.3	8672.5	691.8	691.9
200,000	0.500	0.500	11,161.0	11,439.9	691.9	691.9
500,000	0.500	0.500	16,015.4	16,517.2	692.1	692.1
1,000,000	0.500	0.500	21,051.2	21,821.9	692.2	692.3
2,000,000	0.500	0.500	27,667.0	28,842.8	692.2	692.5
10,000	0.447	0.447	3553.9	3479.9	703.0	703.5
100,000	0.407	0.407	8718.4	8764.5	703.2	702.6
200,000	0.385	0.385	11,454.4	11,584.0	703.3	702.6
500,000	0.347	0.347	16,443.3	16,751.0	703.5	702.7
1,000,000	0.310	0.310	21,618.4	22,145.7	703.6	702.8
2,000,000	0.268	0.268	28,417.3	29,283.9	703.9	702.8

The last parameter to consider is b . We can see from the tables that the value of b is insensitive to the presence of anharmonic terms in the potential. The striking feature of the variation of b for increasing condensate number is that its value increases significantly when cloud–cloud interactions are present over when they are absent. The main driver of this effect occurs at the second split when two clouds become four clouds. Without cloud–cloud interactions, the rate of change of the transverse cloud width ($w_{\perp}(t_1)$) begins to decrease sharply, while this rate of change continues to increase when interactions are present. This leads to a significantly larger value of $w_{\perp}(t_2)$ at the final split.

The b parameter directly measures an effect of the finite-width of the condensate at the time of the final split as shown in Equation (27). It is worth noting that its effect on the value of S_+ is increased for larger rotation speed and, importantly, also for larger interferometer areas. It is therefore possible that this effect may need to be accounted for in the data analysis of the experimental results for larger-area interferometers.

8. Summary and Conclusions

In this work, we have applied a variational model providing approximate solutions to the rotating-frame Gross–Pitaevskii equation to a recent dual-Sagnac atom-interferometry measurement of the lab rotation speed. This measurement involved splitting and recombining a small Bose–Einstein condensate in an ideally harmonic potential. We used the model to study the effects of interactions due to increasing the number of condensate atoms and of the presence of anharmonic terms in the external potential on the operation of the interferometer.

We found that the finite condensate width due to the presence of atom–atom interactions caused a slow decay in the envelope of the variation of the stopped-atom fraction, S_{\pm} , with increasing rotating-frame speed, Ω_z . The rate of this decay is proportional to the square of the width of the condensate at the time of the final split. Thus anything that increases this final width will accelerate the envelope decay rate. This envelope decay rate is also proportional to the interferometer area. Thus, we expect that this effect may be important in state-of-the-art interferometer applications.

In our model, we found that the final width was affected by the breathing motion of the individual clouds caused by self interactions as well as by interactions between different clouds. When a condensate cloud is split in two, the number of atoms in the daughter clouds is roughly half of the original so that the repulsion is reduced while the confinement from the external potential remains the same. Thus, the cloud will begin to contract, increasing the repulsion. Eventually, the contraction stops and the cloud begins expanding until the confinement stops the expansion and contraction begins again. Thus, the self interaction can lead to a bigger or smaller final width. We found that interactions between different clouds can moderate the change in the expansion/contraction rate that happens when a cloud is split. It is possible to minimize the final width by engineering the four-cloud flight time so that the width oscillation is at a minimum.

The amplitude of the envelope of the stopped-atom fraction variation with Ω_z is affected by the presence of anharmonic terms in the potential. This amplitude (parameter a in the study) is decreased when the two overlapping stopped-atom clouds have a relative velocity and/or are not completely overlapped at the final split. The relative velocity can be a combination of the relative velocity of the cloud centers and the expansion or contraction of the cloud width. These effects also decrease when the final width decreases. It is also possible to engineer the trap period to minimize this effect.

Finally, our model predicts that the frequency of the variation of S_{\pm} with Ω_z depends on the Sagnac phase regardless of the presence of interactions and/or anharmonic terms. We found that S_{\pm} varied sinusoidally with the Sagnac phase under all conditions. Thus, it may be possible to use the fit function in Equation (25) to devise a procedure similar to the ellipse-fitting data analysis used in the experiment for common-mode rejection, but which can account for interactions and anharmonic effects.

Author Contributions: Conceptualization, M.E., C.W.C. and C.A.S.; methodology, M.E., C.W.C. and C.A.S.; software, M.E.; validation, S.T., C.S., C.H. and A.S.; formal analysis, S.T., C.S., C.H., A.S. and C.W.C.; investigation, S.T., C.S., C.H., A.S. and C.W.C.; resources, M.E.; data curation, S.T.; writing—original draft preparation, M.E.; writing—review and editing, M.E., C.W.C., C.S., S.T., C.A.S., C.H. and A.S.; visualization, C.H.; supervision, M.E.; project administration, M.E.; funding acquisition, M.E. and C.W.C. All authors have read and agreed to the published version of the manuscript.

Funding: This research was funded by US National Science Foundation grant number 1707776, DARPA grant number FA9453-19-1-0007 and NASA grant number RSA1549080g.

Institutional Review Board Statement: Not applicable.

Informed Consent Statement: Not applicable.

Acknowledgments: The authors would like to thank Jim Stickney for helpful discussions.

Conflicts of Interest: The authors declare no conflict of interest.

Abbreviations

The following abbreviations are used in this manuscript:

AI	Atom Interferometry
BEC	Bose–Einstein condensate
CAL	Cold Atom Laboratory
GPE	Gross–Pitaevskii Equation
LVM	Lagrangian Variational Method
NASA	National Aeronautics and Space Administration
RFGPE	Rotation–frame Gross–Pitaevskii equation
TOP	Time-averaged orbiting potential

Appendix A. Derivation of the Power-Law Equations of Motion

We can derive the variational equations of motion (Equation (5a–d)) for this power-law external potential by inserting Equation (11) into Equation (7b). Thus, we have

$$U_{\text{ext}}^{(3D)}(\mathbf{x}, \mathbf{w}) = \sum_{k=1}^{N_{\text{terms}}} C_{p_x(k), p_y(k), p_z(k)} \sum_{j=1}^{N_c} \left(\frac{1}{\pi^{3/2} w_{jx} w_{jy} w_{jz}} \right) I_{p_x(k)}(x_j, w_{jx}) I_{p_y(k)}(y_j, w_{jy}) I_{p_z(k)}(z_j, w_{jz})$$

where we have defined

$$I_k(\eta_0, w_0) \equiv \int_{-\infty}^{\infty} \eta^k e^{-(\eta-\eta_0)^2/w_0^2} d\eta, \quad k = 0, 1, 2, \dots \quad (\text{A1})$$

Introducing

$$J_k(\eta_0, w_0) \equiv \left(\frac{1}{w_0 \pi^{1/2}} \right) \int_{-\infty}^{\infty} \eta^k e^{-(\eta-\eta_0)^2/w_0^2} d\eta, \quad k = 0, 1, 2, \dots \quad (\text{A2})$$

we can write the variational potential in a compact form. The result is

$$U_{\text{ext}}^{(3D)}(\mathbf{x}, \mathbf{w}) = \sum_{j=1}^{N_c} \sum_{k=1}^{N_{\text{terms}}} C_{p_x(k), p_y(k), p_z(k)} J_{p_x(k)}(x_j, w_{jx}) J_{p_y(k)}(y_j, w_{jy}) J_{p_z(k)}(z_j, w_{jz}) \quad (\text{A3})$$

The integral, $J_k(\eta, w)$, is easily evaluated so it can be written as

$$J_k(\eta, w) = \begin{cases} \sum_{m=0}^{k/2} \left(\frac{k!}{m!(k-2m)!} \right) \eta^{k-2m} \left(\frac{1}{2} w \right)^{2m} & k = \text{even integer} \\ \sum_{m=0}^{(k-1)/2} \left(\frac{k!}{m!(k-2m)!} \right) \eta^{k-2m} \left(\frac{1}{2} w \right)^{2m} & k = \text{odd integer} \end{cases} \quad (\text{A4})$$

We can use this expression to write down the equations of motion.

For the equations of motion we need to compute the derivative of $U_{\text{ext}}(\mathbf{x}, \mathbf{w})$ with respect to the center coordinates and center widths. These are easily done with results

$$\begin{aligned} \frac{\partial U_{\text{ext}}^{(3D)}}{\partial x_j} &= \sum_{k=1}^{N_{\text{terms}}} C_{p_x(k), p_y(k), p_z(k)} \left(\frac{\partial J_{p_x(k)}}{\partial x_j} \right) J_{p_y(k)}(y_j, w_{jy}) J_{p_z(k)}(z_j, w_{jz}) \\ \frac{\partial U_{\text{ext}}^{(3D)}}{\partial y_j} &= \sum_{k=1}^{N_{\text{terms}}} C_{p_x(k), p_y(k), p_z(k)} J_{p_x(k)}(x_j, w_{jx}) \left(\frac{\partial J_{p_y(k)}}{\partial y_j} \right) J_{p_z(k)}(z_j, w_{jz}) \\ \frac{\partial U_{\text{ext}}^{(3D)}}{\partial z_j} &= \sum_{k=1}^{N_{\text{terms}}} C_{p_x(k), p_y(k), p_z(k)} J_{p_x(k)}(x_j, w_{jx}) J_{p_y(k)}(y_j, w_{jy}) \left(\frac{\partial J_{p_z(k)}}{\partial z_j} \right) \end{aligned}$$

$$\begin{aligned}\frac{\partial U_{\text{ext}}^{(3D)}}{\partial w_{jx}} &= \sum_{k=1}^{N_{\text{terms}}} C_{p_x(k), p_y(k), p_z(k)} \left(\frac{\partial J_{p_x(k)}}{\partial w_{jx}} \right) J_{p_y(k)}(y_j, w_{jy}) J_{p_z(k)}(z_j, w_{jz}) \\ \frac{\partial U_{\text{ext}}^{(3D)}}{\partial w_{jy}} &= \sum_{k=1}^{N_{\text{terms}}} C_{p_x(k), p_y(k), p_z(k)} J_{p_x(k)}(x_j, w_{jx}) \left(\frac{\partial J_{p_y(k)}}{\partial w_{jy}} \right) J_{p_z(k)}(z_j, w_{jz}) \\ \frac{\partial U_{\text{ext}}^{(3D)}}{\partial w_{jz}} &= \sum_{k=1}^{N_{\text{terms}}} C_{p_x(k), p_y(k), p_z(k)} J_{p_x(k)}(x_j, w_{jx}) J_{p_y(k)}(y_j, w_{jy}) \left(\frac{\partial J_{p_z(k)}}{\partial w_{jz}} \right).\end{aligned}$$

where the derivatives can be expressed as follows.

$$\frac{\partial J_k}{\partial \eta} = \begin{cases} \sum_{m=0}^{k/2} \left(\frac{k!}{m!(k-2m-1)!} \right) \eta^{k-2m-1} \left(\frac{1}{2} w \right)^{2m} & k = \text{even integer} \\ \sum_{m=0}^{(k-1)/2} \left(\frac{k!}{m!(k-2m-1)!} \right) \eta^{k-2m-1} \left(\frac{1}{2} w \right)^{2m} & k = \text{odd integer} \end{cases} \quad (\text{A5})$$

and where $\eta = x, y, z$ and

$$\frac{\partial J_k}{\partial w} = \begin{cases} \sum_{m=1}^{k/2} \left(\frac{k!}{(m-1)!(k-2m)!} \right) \eta^{k-2m} \left(\frac{1}{2} w \right)^{2m-1} & k = \text{even integer} \\ \sum_{m=1}^{(k-1)/2} \left(\frac{k!}{(m-1)!(k-2m)!} \right) \eta^{k-2m} \left(\frac{1}{2} w \right)^{2m-1} & k = \text{odd integer} \end{cases} \quad (\text{A6})$$

Appendix B. Interaction Terms in the Variational Equations of Motion

The space and width gradients of $U_{\text{int}}^{(3D)}(\mathbf{x}, \mathbf{w})$ appearing in the variational equations of motion are derived in Ref. [60]. The result for the space gradients is

$$F_{j\eta}(\mathbf{x}, \mathbf{w}) \equiv \frac{\partial U_{\text{int}}^{(3D)}}{\partial \eta_j} = \left(\frac{4gN}{(\pi)^{3/2}N_c} \right) \sum_{j'=1}^{N_c} \prod_{\substack{\eta'=x,y,z \\ j' \neq j}} \left(\frac{\exp \left\{ -\frac{(\eta'_j - \eta_j)^2}{w_{j'\eta'}^2 + w_{j\eta}^2} \right\}}{(w_{j'\eta'}^2 + w_{j\eta}^2)^{1/2}} \right) \left(\frac{\eta'_j - \eta_j}{w_{j'\eta'}^2 + w_{j\eta}^2} \right), \quad (\text{A7})$$

where $\eta = x, y, z$.

It is worth noting that this quantity describes the “force” exerted on cloud j due to all of the other clouds $j' \neq j$ and is only non-zero when there is significant overlap between two different clouds. It is also notable that the force of cloud j' acting on cloud j is equal and opposite to the force of cloud j on j' as can be seen from the above equation. Thus, all of the cloud–cloud interactions obey a “Newton’s Third Law” condition.

The equations of motion contain terms are twice the width gradient of $U_{\text{int}}^{(3D)}(\mathbf{x}, \mathbf{w})$. These can be written in the following form:

$$2 \frac{\partial U_{\text{int}}}{\partial w_{j\eta}} \equiv - \frac{gN}{(2\pi)^{3/2}N_c} \left(\frac{1}{w_{jx}w_{jy}w_{jz}w_{j\eta}} \right) + W_{j\eta}(\mathbf{x}, \mathbf{w}), \quad \eta = x, y, z. \quad (\text{A8})$$

where the first term accounts for the self-interaction of cloud j . The second term accounts for the interaction of cloud j with the other clouds and has the form [60]

$$W_{j\eta}(\mathbf{x}, \mathbf{w}) \equiv \frac{4gN}{(\pi)^{3/2}N_c} \sum_{j'=1}^{N_c} \prod_{\substack{\eta'=x,y,z \\ j' \neq j}} \left(\frac{\exp \left\{ -\frac{(\eta'_j - \eta_j)^2}{w_{j'\eta'}^2 + w_{j\eta}^2} \right\}}{(w_{j'\eta'}^2 + w_{j\eta}^2)^{1/2}} \right) \left(\frac{w_{j\eta} \left(2(\eta'_j - \eta_j)^2 - (w_{j'\eta'}^2 + w_{j\eta}^2) \right)}{(w_{j'\eta'}^2 + w_{j\eta}^2)^2} \right). \quad (\text{A9})$$

Note that this term is negligible unless cloud j overlaps one or more of the other clouds, $j' \neq j$.

References

1. Bongs, K.; Holynski, M.; Vovrosh, J.; Bouyer, P.; Condon, G.; Rasel, E.; Schubert, C.; Schleich, W.P.; Roura, A. Taking atom interferometric quantum sensors from the laboratory to real-world applications. *Nat. Rev. Phys.* **2019**, *1*, 731–739. [\[CrossRef\]](#)
2. Richard, H.P.; Yu, C.; Zhong, W.; Estey, B.; Maller, H. Measurement of the fine-structure constant as a test of the standard model. *Science* **2018**, *360*, 6385.
3. Weiss, D.S.; Young, B.C.; Chu, S. Precision measurement of the photon recoil of an atom using atomic interferometry. *Phys. Rev. Lett.* **1993**, *70*, 2706–2709. [\[CrossRef\]](#) [\[PubMed\]](#)
4. Bouchendira, R.; Cladé, P.; Guellati-Khélifa, S.; Nez, F.M.C.; Biraben, F.M.C. New Determination of the Fine Structure Constant and Test of the Quantum Electrodynamics. *Phys. Rev. Lett.* **2011**, *106*, 080801. [\[CrossRef\]](#) [\[PubMed\]](#)
5. Hanneke, D.; Fogwell, S.; Gabrielse, G. New Measurement of the Electron Magnetic Moment and the Fine Structure Constant. *Phys. Rev. Lett.* **2008**, *100*, 120801. [\[CrossRef\]](#) [\[PubMed\]](#)
6. Rosi, G.; Sorrentino, F.; Cacciapuoti, L.; Prevedelli, M.; Tino, G.M. Precision measurement of the Newtonian gravitational constant using cold atoms. *Nature* **2014**, *510*, 518–521. [\[CrossRef\]](#) [\[PubMed\]](#)
7. Fixler, J.B.; Foster, G.T.; McGuirk, J.M.; Kasevich, M.A. Atom interferometer measurement of the Newtonian constant of gravity. *Science* **2007**, *315*, 74–77. [\[CrossRef\]](#)
8. Ménotet, V.; Vermeulen, P.; Le Moigne, N.; Bonvalot, S.; Bouyer, P.; Landragin, A.; Desruelle, B. Gravity measurements below 10^{-9} g with a transportable absolute quantum gravimeter. *Sci. Rep.* **2018**, *8*, 12300. [\[CrossRef\]](#)
9. Geneves, G.; Gournay, P.; Gosset, A.; Lecollinet, M.; Villar, F.; Pinot, P.; Juncar, P.; Clairon, A.; Landragin, A.; Holleville, D.; et al. The BNM Watt balance project. *IEEE Trans. Instrum. Meas.* **2005**, *54*, 850–853. [\[CrossRef\]](#)
10. Andreas, B.; Azuma, Y.; Bartl, G.; Becker, P.; Bettin, H.; Borys, M.; Busch, I.; Gray, M.; Fuchs, P.; Fujii, K.; et al. Determination of the Avogadro Constant by Counting the Atoms in a ^{28}Si Crystal. *Phys. Rev. Lett.* **2011**, *106*, 030801. [\[CrossRef\]](#)
11. Bonnín, A.; Zahzam, N.; Bidel, Y.; Bresson, A. Simultaneous dual-species matter-wave accelerometer. *Phys. Rev. A* **2013**, *88*, 043615. [\[CrossRef\]](#)
12. Dickerson, S.M.; Hogan, J.M.; Sugarbaker, A.; Johnson, D.M.S.; Kasevich, M.A. Multiaxis Inertial Sensing with Long-Time Point Source Atom Interferometry. *Phys. Rev. Lett.* **2013**, *111*, 083001. [\[CrossRef\]](#) [\[PubMed\]](#)
13. Barrett, B.; Antoni-Micollier, L.; Chichet, L.; Battelier, B.; Lévêque, T.; Landragin, A.; Bouyer, P. Dual matter-wave inertial sensors in weightlessness. *Nat. Commun.* **2016**, *7*, 13786. [\[CrossRef\]](#) [\[PubMed\]](#)
14. Antoine, C.; Bord, C.J. Quantum theory of atomic clocks and gravito-inertial sensors: An update. *J. Opt. B Quantum Semiclass. Opt.* **2003**, *5*, S199–S207. [\[CrossRef\]](#)
15. Geiger, R.; Ménotet, V.; Stern, G.; Zahzam, N.; Cheinet, P.; Battelier, B.; Villing, A.; Moron, F.; Lours, M.; Bidel, Y.; et al. Detecting inertial effects with airborne matter-wave interferometry. *Nat. Commun.* **2011**, *2*, 474. [\[CrossRef\]](#)
16. Moan, E.R.; Horne, R.A.; Arpornthip, T.; Luo, Z.; Fallon, A.J.; Berl, S.J.; Sackett, C.A. Quantum Rotation Sensing with Dual Sagnac Interferometers in an Atom-Optical Waveguide. *Phys. Rev. Lett.* **2020**, *124*, 120403. [\[CrossRef\]](#)
17. Zhou, L.; Xiong, Z.; Yang, W.; Tang, B.; Peng, W.; Hao, K.; Li, R.; Liu, M.; Wang, J.L.; Zhan, M. Development of an atom gravimeter and status of the 10-m atom interferometer for precision gravity measurement. *Gen. Relativ. Gravit.* **2011**, *43*, 1931–1942. [\[CrossRef\]](#)
18. Dimopoulos, S.; Graham, P.W.; Hogan, J.M.; Kasevich, M.A.; Rajendran, S. Atomic gravitational wave interferometric sensor. *Phys. Rev. D* **2008**, *78*, 122002. [\[CrossRef\]](#)
19. Hogan, J.M.; Kasevich, M.A. Atom-interferometric gravitational-wave detection using heterodyne laser links. *Phys. Rev. A* **2016**, *94*, 033632. [\[CrossRef\]](#)
20. Hogan, J.M.; Johnson, D.M.S.; Dickerson, S.; Kovachy, T.; Sugarbaker, A.; Chiow, S.W.; Graham, P.W.; Kasevich, M.A.; Saif, B.; Rajendran, S.; et al. An atomic gravitational wave interferometric sensor in low earth orbit (AGIS-LEO). *Gen. Relativ. Gravit.* **2011**, *43*, 1953–2009. [\[CrossRef\]](#)
21. Amaro-Seoane, P.; Aoudia, S.; Babak, S.; Binétruy, P.; Berti, E.; Bohé, A.; Caprini, C.; Colpi, M.; Cornish, N.J.; Danzmann, K.; et al. Low-frequency gravitational-wave science with eLISA/NGO. *Class. Quantum Gravity* **2012**, *29*, 124016. [\[CrossRef\]](#)
22. Chaibi, W.; Geiger, R.; Canuel, B.; Bertoldi, A.; Landragin, A.; Bouyer, P. Low frequency gravitational wave detection with ground-based atom interferometer arrays. *Phys. Rev. D* **2016**, *93*, 021101. [\[CrossRef\]](#)
23. Hamilton, P.; Jaffe, M.; Haslinger, P.; Simmons, Q.; Müller, H.; Khoury, J. Atom-interferometry constraints on dark energy. *Science* **2015**, *349*, 849–851. [\[CrossRef\]](#)
24. Jaffe, M.; Haslinger, P.; Xu, V.; Hamilton, P.; Upadhye, A.; Elder, B.; Khoury, J.; Müller, H. Testing sub-gravitational forces on atoms from a miniature in-vacuum source mass. *Nat. Phys.* **2017**, *13*, 938–942. [\[CrossRef\]](#)
25. Strigari, L.E. Galactic searches for dark matter. *Phys. Rep.* **2013**, *531*, 1–88. [\[CrossRef\]](#)
26. Arvanitaki, A.; Graham, P.W.; Hogan, J.M.; Rajendran, S.; Van Tilburg, K. Search for light scalar dark matter with atomic gravitational wave detectors. *Phys. Rev. D* **2018**, *97*, 075020. [\[CrossRef\]](#)
27. Hees, A.; Guéna, J.; Abgrall, M.; Bize, S.; Wolf, P. Searching for an Oscillating Massive Scalar Field as a Dark Matter Candidate Using Atomic Hyperfine Frequency Comparisons. *Phys. Rev. Lett.* **2016**, *117*, 061301. [\[CrossRef\]](#) [\[PubMed\]](#)
28. Overstreet, C.; Asenbaum, P.; Kovachy, T.; Notermans, R.; Hogan, J.M.; Kasevich, M.A. Effective Inertial Frame in an Atom Interferometric Test of the Equivalence Principle. *Phys. Rev. Lett.* **2018**, *120*, 183604. [\[CrossRef\]](#)

29. Elder, B.; Khoury, J.; Haslinger, P.; Jaffe, M.; Müller, H.; Hamilton, P. Chameleon dark energy and atom interferometry. *Phys. Rev. D* **2016**, *94*, 044051. [\[CrossRef\]](#)
30. Niebauer, T.M.; McHugh, M.P.; Faller, J.E. Galilean test for the fifth force. *Phys. Rev. Lett.* **1987**, *59*, 609–612. [\[CrossRef\]](#)
31. Touboul, P.; Métris, G.; Rodrigues, M.; André, Y.; Baghi, Q.; Bergé, J.; Boulanger, D.; Bremer, S.; Carle, P.; Chhun, R.; et al. MICROSCOPE Mission: First Results of a Space Test of the Equivalence Principle. *Phys. Rev. Lett.* **2017**, *119*, 231101. [\[CrossRef\]](#)
32. Fray, S.; Diez, C.A.; Hänsch, T.W.; Weitz, M. Atomic Interferometer with Amplitude Gratings of Light and Its Applications to Atom Based Tests of the Equivalence Principle. *Phys. Rev. Lett.* **2004**, *93*, 240404. [\[CrossRef\]](#) [\[PubMed\]](#)
33. Tarallo, M.G.; Mazzoni, T.; Poli, N.; Sutyryn, D.V.; Zhang, X.; Tino, G.M. Test of Einstein Equivalence Principle for 0-Spin and Half-Integer-Spin Atoms: Search for Spin-Gravity Coupling Effects. *Phys. Rev. Lett.* **2014**, *113*, 023005. [\[CrossRef\]](#) [\[PubMed\]](#)
34. Schlippert, D.; Hartwig, J.; Albers, H.; Richardson, L.L.; Schubert, C.; Roura, A.; Schleich, W.P.; Ertmer, W.; Rasel, E.M. Quantum Test of the Universality of Free Fall. *Phys. Rev. Lett.* **2014**, *112*, 203002. [\[CrossRef\]](#)
35. Rosi, G.; D’Amico, G.; Cacciapuoti, L.; Sorrentino, F.; Prevedelli, M.; Zych, M.; Brukner, Č.; Tino, G.M. Quantum test of the equivalence principle for atoms in coherent superposition of internal energy states. *Nat. Commun.* **2017**, *8*, 15529. [\[CrossRef\]](#) [\[PubMed\]](#)
36. Geiger, R.; Trupke, M. Proposal for a Quantum Test of the Weak Equivalence Principle with Entangled Atomic Species. *Phys. Rev. Lett.* **2018**, *120*, 043602. [\[CrossRef\]](#)
37. Andrews, M.R.; Townsend, C.G.; Miesner, H.J.; Durfee, D.S.; Kurn, D.M.; Ketterle, W. Observation of Interference Between Two Bose Condensates. *Science* **1997**, *275*, 637–641. [\[CrossRef\]](#)
38. Simsarian, J.E.; Denschlag, J.; Edwards, M.; Clark, C.W.; Deng, L.; Hagley, E.W.; Helmerson, K.; Rolston, S.L.; Phillips, W.D. Imaging the Phase of an Evolving Bose–Einstein Condensate Wave Function. *Phys. Rev. Lett.* **2000**, *85*, 2040–2043. [\[CrossRef\]](#)
39. Hagley, E.W.; Deng, L.; Kozuma, M.; Trippenbach, M.; Band, Y.B.; Edwards, M.; Doery, M.; Julienne, P.S.; Helmerson, K.; Rolston, S.L.; et al. Measurement of the Coherence of a Bose–Einstein Condensate. *Phys. Rev. Lett.* **1999**, *83*, 3112–3115. [\[CrossRef\]](#)
40. Gupta, S.; Dieckmann, K.; Hadzibabic, Z.; Pritchard, D.E. Contrast Interferometry using Bose–Einstein Condensates to Measure \hbar/m and α . *Phys. Rev. Lett.* **2002**, *89*, 140401. [\[CrossRef\]](#)
41. Debs, J.E.; Altin, P.A.; Barter, T.H.; Döring, D.; Dennis, G.R.; McDonald, G.; Anderson, R.P.; Close, J.D.; Robins, N.P. Cold-atom gravimetry with a Bose–Einstein condensate. *Phys. Rev. A* **2011**, *84*, 033610. [\[CrossRef\]](#)
42. Abend, S.; Gebbe, M.; Gersemann, M.; Ahlers, H.; Müntinga, H.; Giese, E.; Gaaloul, N.; Schubert, C.; Lämmerzahl, C.; Ertmer, W.; et al. Atom-Chip Fountain Gravimeter. *Phys. Rev. Lett.* **2016**, *117*, 203003. [\[CrossRef\]](#)
43. Bell, T.A.; Glidden, J.A.P.; Humbert, L.; Bromley, M.W.J.; Haine, S.A.; Davis, M.J.; Neely, T.W.; Baker, M.A.; Rubinsztein-Dunlop, H. Bose–Einstein condensation in large time-averaged optical ring potentials. *New J. Phys.* **2016**, *18*, 035003. [\[CrossRef\]](#)
44. Pandey, S.; Mas, H.; Drougakis, G.; Thekkepatt, P.; Bolpasi, V.; Vasilakis, G.; Poullos, K.; von Klitzing, W. Hypersonic Bose–Einstein condensates in accelerator rings. *Nature* **2019**, *570*, 205–209. [\[CrossRef\]](#) [\[PubMed\]](#)
45. Turpin, A.; Polo, J.; Loiko, Y.V.; Küber, J.; Schmaltz, F.; Kalkandjiev, T.K.; Ahufinger, V.; Birkel, G.; Mompart, J. Blue-detuned optical ring trap for Bose–Einstein condensates based on conical refraction. *Opt. Express* **2015**, *23*, 1638–1650. [\[CrossRef\]](#) [\[PubMed\]](#)
46. de Goër de Herve, M.; Guo, Y.; Rossi, C.D.; Kumar, A.; Badr, T.; Dubessy, R.; Longchambon, L.; Perrin, H. A versatile ring trap for quantum gases. *J. Phys. B At. Mol. Opt. Phys.* **2021**, *54*, 125302. [\[CrossRef\]](#)
47. Ryu, C.; Boshier, M.G. Integrated coherent matter wave circuits. *New J. Phys.* **2016**, *17*, 092002. [\[CrossRef\]](#)
48. Becker, D.; Lachmann, M.D.; Seidel, S.T.; Ahlers, H.; Dinkelaker, A.N.; Grosse, J.; Hellmig, O.; Müntinga, H.; Schkolnik, V.; Wendrich, T.; et al. Space-borne Bose–Einstein condensation for precision interferometry. *Nature* **2018**, *562*, 391–395. [\[CrossRef\]](#)
49. Frye, K.; Abend, S.; Bartosch, W.; Bawamia, A.; Becker, D.; Blume, H.; Braxmaier, C.; Chiow, S.W.; Efremov, M.A.; Ertmer, W.; et al. The Bose–Einstein Condensate and Cold Atom Laboratory. *EPJ Quantum Technol.* **2021**, *8*, 1. [\[CrossRef\]](#)
50. Aveline, D.C.; Williams, J.R.; Elliott, E.R.; Dutenhoffer, C.; Kellogg, J.R.; Kohel, J.M.; Lay, N.E.; Oudrhiri, K.; Shotwell, R.F.; Yu, N.; et al. Observation of Bose–Einstein condensates in an Earth-orbiting research lab. *Nature* **2020**, *582*, 193–197; Erratum in *Nature* **2020**, *584*, E1. [\[CrossRef\]](#)
51. Elliott, E.R.; Krutzik, M.C.; Williams, J.R.; Thompson, R.J.; Aveline, D.C. NASA’s Cold Atom Lab (CAL): System development and ground test status. *NPJ Microgravity* **2018**, *4*, 16. [\[CrossRef\]](#) [\[PubMed\]](#)
52. Jamison, A.O.; Kutz, J.N.; Gupta, S. Atomic interactions in precision interferometry using Bose–Einstein condensates. *Phys. Rev. A* **2011**, *84*, 043643. [\[CrossRef\]](#)
53. Grond, J.; Hohenester, U.; Mazets, I.; Schmiedmayer, J. Atom interferometry with trapped Bose–Einstein condensates: Impact of atom–atom interactions. *New J. Phys.* **2010**, *12*, 065036. [\[CrossRef\]](#)
54. Benton, B.; Krygier, M.; Heward, J.; Edwards, M.; Clark, C.W. Prototyping method for Bragg-type atom interferometers. *Phys. Rev. A* **2011**, *84*, 043648. [\[CrossRef\]](#)
55. Olshanii, M.; Dunjko, V. Interferometry in dense nonlinear media and interaction-induced loss of contrast in microfabricated atom interferometers. *arXiv* **2005**, arXiv:cond-mat/0505358.
56. Stickney, J.A.; Kaffle, R.P.; Anderson, D.Z.; Zozulya, A.A. Theoretical analysis of a single- and double-reflection atom interferometer in a weakly confining magnetic trap. *Phys. Rev. A* **2008**, *77*, 043604. [\[CrossRef\]](#)
57. Impens, F. Hidden symmetry and nonlinear paraxial atom optics. *Phys. Rev. A* **2009**, *80*, 063617. [\[CrossRef\]](#)
58. Pitaevskii, L.; Stringari, S. *Bose–Einstein Condensation*; Oxford University Press: Oxford, UK, 2003.
59. Antoine, X.; Bao, W.; Besse, C. Computational methods for the dynamics of the nonlinear Schrödinger/Gross–Pitaevskii equations. *Comput. Phys. Commun.* **2013**, *184*, 2621–2633. [\[CrossRef\]](#)

60. Ashwood, E.; Wells, E.W.; Kurkcuoglu, D.M.; Sapp, R.C.; Clark, C.W.; Edwards, M. Tools for designing atom interferometers in a microgravity environment. *Phys. Rev. A* **2019**, *99*, 043615. [[CrossRef](#)]
61. Pérez-García, V.M.; Michinel, H.; Cirac, J.I.; Lewenstein, M.; Zoller, P. Low Energy Excitations of a Bose–Einstein Condensate: A Time-Dependent Variational Analysis. *Phys. Rev. Lett.* **1996**, *77*, 5320–5323. [[CrossRef](#)]
62. Pérez-García, V.M.; Michinel, H.; Cirac, J.I.; Lewenstein, M.; Zoller, P. Dynamics of Bose–Einstein condensates: Variational solutions of the Gross–Pitaevskii equations. *Phys. Rev. A* **1997**, *56*, 1424–1432. [[CrossRef](#)]
63. Carretero-González, R.; Anderson, B.P.; Kevrekidis, P.G.; Frantzeskakis, D.J.; Weiler, C.N. Dynamics of vortex formation in merging Bose–Einstein condensate fragments. *Phys. Rev. A* **2008**, *77*, 033625. [[CrossRef](#)]
64. Yang, T.; Xiong, B.; Benedict, K.A. Dynamical excitations in the collision of two-dimensional Bose–Einstein condensates. *Phys. Rev. A* **2013**, *87*, 023603. [[CrossRef](#)]
65. Xiong, B.; Yang, T.; Benedict, K.A. Distortion of interference fringes and the resulting vortex production of merging Bose–Einstein condensates. *Phys. Rev. A* **2013**, *88*, 043602. [[CrossRef](#)]
66. Mukherjee, K.; Mukherjee, K.; Mistakidis, S.; Kevrekidis, P.G.; Schmelcher, P. Quench induced vortex-bright-soliton formation in binary Bose–Einstein condensates. *J. Phys. B At. Mol. Opt. Phys.* **2020**, *53*, 055302. [[CrossRef](#)]
67. Moan, E.; Berl, S.; Luo, Z.; Sackett, C.A. Controlling the anharmonicity of a time-orbiting potential trap. In *Optical, Opto-Atomic, and Entanglement-Enhanced Precision Metrology II*; Shahriar, S.M., Scheuer, J., Eds.; International Society for Optics and Photonics, SPIE: Stockholm, Sweden, 2020; Volume 11296, pp. 238–245. [[CrossRef](#)]